

Evidence that the Hot Jupiter WASP-77 A b Formed Beyond Its Parent Protoplanetary Disk's H₂O Ice Line

HENRIQUE REGGIANI ^{1,*} KEVIN C. SCHLAUFMAN ² BRIAN F. HEALY ² JOSHUA D. LOTHRINGER ³ AND
DAVID K. SING ^{2,4}

¹*The Observatories of the Carnegie Institution for Science, 813 Santa Barbara St, Pasadena, CA 91101, USA*

²*William H. Miller III Department of Physics and Astronomy, Johns Hopkins University, 3400 N Charles St, Baltimore, MD 21218, USA*

³*Department of Physics, Utah Valley University, College of Science - MS 179, 800 W University Pkwy, Orem, UT 84058, USA*

⁴*Department of Earth and Planetary Sciences, Johns Hopkins University, 3400 N Charles St, Baltimore, MD 21218, USA*

(Received December 28, 2021; Accepted January 18, 2022)

Accepted for publication in the *Astronomical Journal*

ABSTRACT

Idealized protoplanetary disk and giant planet formation models have been interpreted to suggest that a giant planet's atmospheric abundances can be used to infer its formation location in its parent protoplanetary disk. It has recently been reported that the hot Jupiter WASP-77 A b has sub-solar atmospheric carbon and oxygen abundances with a solar C/O abundance ratio. Assuming solar carbon and oxygen abundances for its host star WASP-77 A, WASP-77 A b's atmospheric carbon and oxygen abundances possibly indicate that it accreted its envelope interior to its parent protoplanetary disk's H₂O ice line from carbon-depleted gas with little subsequent planetesimal accretion or core erosion. We comprehensively model WASP-77 A and use our results to better characterize WASP-77 A b. We show that the photospheric abundances of carbon and oxygen in WASP-77 A are super-solar with a sub-solar C/O abundance ratio, implying that WASP-77 A b's atmosphere has significantly sub-stellar carbon and oxygen abundances with a super-stellar C/O ratio. Our result possibly indicates that WASP-77 A b's envelope was accreted by the planet beyond its parent protoplanetary disk's H₂O ice line. While numerous theoretical complications to these idealized models have now been identified, the possibility of non-solar protoplanetary disk abundance ratios confound even the most sophisticated protoplanetary disk and giant planet formation models. We therefore argue that giant planet atmospheric abundance ratios can only be meaningfully interpreted relative to the possibly non-solar mean compositions of their parent protoplanetary disks as recorded in the photospheric abundances of their solar-type dwarf host stars.

Keywords: Exoplanet astronomy(486) — Exoplanet atmospheric composition(2021) — Exoplanet formation(492) — Exoplanet migration(2205) — Exoplanet systems(484) — Exoplanet tides(497) — Exoplanets(498) — Hot Jupiters(753) — Planet hosting stars(1242) — Star-planet interactions(2177) — Stellar abundances(1577)

1. INTRODUCTION

It has been proposed that a giant planet's formation location in its parent protoplanetary disk can be dis-

cerned by studying the abundances of the elements in the planet's atmosphere. While acknowledging the importance of planetesimal accretion after runaway envelope accretion in determining giant planet envelope abundances, based on static disk models Öberg et al. (2011) suggested that stellar C/O abundance ratios should be realized for giant planets forming inside both their parent protoplanetary disks' H₂O ice and carbon-grain sublimation lines where all volatiles are in the gas

Corresponding author: Henrique Reggiani
hreggiani@carnegiescience.edu

* Carnegie Fellow

phase. Sub-stellar or stellar C/O abundance ratios combined with super-stellar carbon abundances were argued to result from the accretion of large amounts of icy planetesimals after envelope accretion. Super-stellar C/O abundance ratios and carbon abundances could be attributed either to formation close to the CO₂ or CO ice lines or by the accretion of carbon-rich grains in the narrow range inside the H₂O ice line but outside the carbon-grain sublimation line. Super-stellar C/O abundance ratios and sub-stellar carbon and oxygen abundances were put forward as a unique signature of formation beyond the H₂O ice line.

This straightforward scenario outlined for the case of static disks is significantly complicated in more realistic models that include disk chemical & structural evolution, the radial migration of solids, detailed models for planetesimal accretion, and/or post envelope-accretion migration. The locations of the H₂O, CO₂, and CO ice lines depend on stellar luminosity and move inward with time as a viscously evolving disk’s mass accretion rate declines (e.g., Harsono et al. 2015). The inclusion of radially migrating solids in viscously evolving disks can also cause the H₂O ice line to move in by a factor of two (Piso et al. 2015). In this case, the C/O abundance ratio in disk gas is most likely to be super-stellar between the CO₂ and CO ice lines (Piso et al. 2015). Gas drag, sublimation, vapor diffusion, condensation, and coagulation on major carbon- and oxygen-bearing volatiles indicate that giant planets that accreted their envelopes inside the H₂O ice line should have super-stellar C/O (Ali-Dib et al. 2014; Ali-Dib 2017). In the absence of core erosion, pebble accretion is thought to produce sub-stellar carbon and oxygen abundances but super-stellar C/O abundance ratios (e.g., Madhusudhan et al. 2017; Booth et al. 2017). The point in time during a disk’s evolution at which a giant planet forms also affects the C/O abundance ratio of its envelope (Cridland et al. 2016). Chemical evolution in disks can mask the influence of formation location on envelope composition though (Eistrup et al. 2018), with super-stellar C/O only realized between CO₂ and CH₄ ice lines and greater giant planet envelope abundance dispersions expected in more metal-rich disks (Cridland et al. 2020; Notsu et al. 2020). High-eccentricity migration after disk dissipation can lead to sub-stellar carbon and oxygen abundances with stellar or super-stellar C/O abundance ratios (Madhusudhan et al. 2014). For ultra-hot Jupiters, atmospheric abundances of refractory elements like magnesium, silicon, and iron also can constrain formation location (e.g., Lothringer et al. 2021).

It has also been argued that the abundances in giant planet envelopes depend critically on the assumptions

made regarding the refractory composition of the inner disk (Mordasini et al. 2016; Cridland et al. 2019a, 2020). Compositions inherited from the interstellar medium but including the destruction of carbon grains in the inner disk by oxidizing reactions on grain surfaces require C/O < 1, both inside and outside the H₂O ice line. The reason is that the accretion of oxygen in the form of silicate planetesimals in the former case and H₂O-rich material in the latter case drive C/O below its abundance in disk gas at a giant planet’s formation location. In contrast, the assumptions that solids form along the condensation sequence as a disk cools can still produce giant planet envelopes with C/O > 1.

All of these analyses rely on two assumptions: (1) that the envelope of a young giant planet stays well mixed during its formation even though most metals are accreted before most gas and (2) that a mature giant planet’s atmosphere has a similar composition to the average composition of its envelope at the end of the planet formation process. While fully convective and therefore well-mixed envelopes are the usual outcome of giant planet formation models, compositional gradients can quench convection (e.g., Leconte & Chabrier 2012). In this case, the abundances in a giant planet’s envelope will only reflect the abundances of the gas it accreted during runaway accretion (Thiabaud et al. 2015). Despite all of these complications, one robust prediction of giant planet formation models in dynamically evolving disks is that the metal abundances of giant planets with $M_p \lesssim 2 M_{Jup}$ are dominated by the accretion of planetesimals after envelope accretion. On the other hand, the metal abundances of giant planets with $M_p \gtrsim 2 M_{Jup}$ are dominated by envelope accretion itself (Mordasini et al. 2014, 2016; Cridland et al. 2019b).

In short, the interpretation of giant planet atmospheric carbon, oxygen, and C/O abundances is far from simple. Moreover, giant planet atmospheric abundance ratios can only be meaningfully interpreted relative to the mean compositions of their parent protoplanetary disk. Because the protoplanetary disks that formed the observed giant planets disappeared long ago, the only way to reveal the mean compositions of those disks is to use the photospheric abundances of their host stars. During the era of giant planet formation, the star growing at the center of a protoplanetary disk has already accreted 99% of the material that ever passed through its disk. As a result, the photospheric abundances of solar-type planet-host stars are an excellent proxy for mean protoplanetary disk abundances. The implication is that accurate and precise host star elemental abundances for the same elements observed in giant planet atmospheres are critically needed to achieve the full po-

tential of giant planet atmospheric abundance inferences as planet formation constraints.

In this article, we infer photospheric and fundamental stellar parameters as well as individual elemental abundances—including carbon and oxygen—for the hot Jupiter host star WASP-77 A. Atmospheric carbon and oxygen abundances for the hot Jupiter WASP-77 A b were recently published by [Line et al. \(2021\)](#), and the carbon and oxygen abundances we infer for WASP-77 A qualitatively change the interpretation of WASP-77 A b's atmospheric abundances. We describe in [Section 2](#) the high-resolution optical spectrum we collected for WASP-77 A. We then infer stellar parameters from that spectrum and all available astrometric and photometric data in [Section 3](#). We derive the individual elemental abundance in WASP-77 A's photosphere in [Section 4](#). We infer updated parameters for the planet WASP-77 A b that are self consistent with the stellar parameters we inferred for its host star in [Section 5](#). We review our results and their implications in [Section 6](#). We conclude by summarizing our findings in [Section 7](#).

2. DATA

The hot Jupiter host star WASP-77 A has right ascension $\alpha = 02\ 28\ 37.23$, declination $\delta = -07\ 03\ 38.4$, and is also known as BD-07 436 A, TYC 4697-201-1, TOI-398, and Gaia EDR3 5178405479961698048. We observed it from Apache Point Observatory (APO) with the Astrophysical Research Consortium (ARC) 3.5-m Telescope and its ARC Echelle Spectrograph (ARCES; [Wang et al. 2003](#)) for 750 seconds starting at UTC 2021 February 23 01:42:55. We used the standard 1''6 x 3''2 slit, yielding a spectrum between 320 nm and 1000 nm with spectral resolution $R \approx 31,500$. We collected all calibration data (e.g., bias, quartz flat field, and ThAr lamp frames) in the late afternoon before the start of our observations. We reduced the raw spectra and calibration frames using a customized version of the CERES echelle spectrograph data reduction package¹ ([Brahm et al. 2017](#)). We cross-correlated each order with a theoretical solar spectrum and averaged the result to calculate the barycentric radial velocity $v_r = 2 \pm 1$ km s⁻¹ consistent with the High Accuracy Radial velocity Planet Searcher (HARPS)-based radial velocity presented in [Maxted et al. \(2013\)](#). We then used our radial velocity measurement to place the normalized spectrum in its rest frame. Because WASP-77 A is a solar-type star with close-to-solar photospheric stellar parameters, we used *iSpec*² ([Blanco-Cuaresma et al. 2014](#); [Blanco-](#)

[Cuaresma 2019](#)) and a solar template spectrum to continuum normalize the individual orders. Our reduced, continuum-normalized one-dimensional (1D) spectrum has a signal-to-noise ratio $S/N \gtrsim 100$ pixel⁻¹ at 500 nm and $S/N \gtrsim 150$ pixel⁻¹ at 620 nm.

3. STELLAR PARAMETERS

We derive photospheric and fundamental stellar parameters for WASP-77 A using the algorithm described in [Reggiani et al. \(2020, 2021\)](#) that makes use of both the classical spectroscopy-only approach³ and isochrones to infer accurate, precise, and self-consistent photospheric and fundamental stellar parameters. Isochrones are especially useful for effective temperature T_{eff} inferences in this case, as high-quality multiwavelength photometry from the ultraviolet to the red optical are available from Data Release (DR2) of the SkyMapper Southern Survey (SMSS) and Gaia DR2. Similarly, the Gaia EDR3 parallax-based distance of WASP-77 A makes the calculation of surface gravity $\log g$ via isochrones straightforward. With both T_{eff} and $\log g$ available via isochrones, the equivalent widths of iron lines can be used to self-consistently determine metallicity [Fe/H] and microturbulence ξ by minimizing the dependence of individual line-based iron abundance inferences on reduced equivalent width.

The inputs to our photospheric and fundamental stellar parameter inference include the equivalent widths of Fe I and Fe II atomic absorption lines, multiwavelength photometry, a Gaia parallax, and an extinction estimate. Using atomic absorption line data from [Yana Galarza et al. \(2019\)](#) for lines from [Meléndez et al. \(2014\)](#) found to be insensitive to stellar activity, we first measure these equivalent widths by fitting Gaussian profiles with the `splot` task in IRAF to our continuum-normalized spectrum. Whenever necessary, we use the `deblend` task to disentangle absorption lines from adjacent spectral features. We gather u , v , g , r , and z photometry and their uncertainties from SMSS DR2 ([Onken et al. 2019](#)) as well as G photometry and its uncertainty from Gaia DR2 ([Gaia Collaboration et al. 2016, 2018](#); [Arenou et al. 2018](#); [Evans et al. 2018](#); [Hambly et al. 2018](#); [Riello et al. 2018](#)). We use a Gaia EDR3 parallax and its uncertainty ([Gaia Collaboration et al. 2021](#); [Fabricius et al. 2021](#); [Lindgren et al. 2021a,b](#); [Torra et al. 2021](#)) as well as an extinction A_V inference based

¹ <https://github.com/rabrahm/ceres>

² <https://www.blancocuaresma.com/s/iSpec>

³ The classical spectroscopy-only approach to photospheric stellar parameter estimation involves simultaneously minimizing for individual line-based iron abundance inferences the difference between Fe I & Fe II-based abundances as well as their dependencies on transition excitation potential and measured reduced equivalent width.

on three-dimensional (3D) maps of extinction in the solar neighborhood from the Structuring by Inversion the Local Interstellar Medium (Stilism) program (Lallement et al. 2014, 2018; Capitanio et al. 2017).

We assume Asplund et al. (2021) solar abundances and use these inputs to infer photospheric and fundamental stellar parameters using the following steps.

1. We use 1D plane-parallel solar-composition ATLAS9 model atmospheres (Castelli & Kurucz 2003), the 2019 version of the MOOG radiative transfer code (Snedden 1973), and the q² MOOG wrapper⁴ (Ramírez et al. 2014) to derive an initial set of photospheric stellar parameters T_{eff} , $\log g$, $[\text{Fe}/\text{H}]$, and ξ using the classical spectroscopy-only approach.
2. We then use the **isochrones** package⁵ (Morton 2015) to fit the MESA Isochrones and Stellar Tracks (MIST; Dotter 2016; Choi et al. 2016; Paxton et al. 2011, 2013, 2015, 2018, 2019) library to our photospheric stellar parameters as well as our input multiwavelength photometry, parallax, and extinction data using MultiNest⁶ (Feroz & Hobson 2008; Feroz et al. 2009, 2019) via PyMultiNest (Buchner et al. 2014). We restricted the MIST library to extinctions in the range $0 \text{ mag} \leq A_V \leq 0.05 \text{ mag}$ based on the maximum plausible A_V value suggested by Stilism. This produces a new set of photospheric and fundamental stellar parameter posteriors that are both self-consistent and physically consistent with stellar evolution.
3. We next impose the posterior-median T_{eff} and $\log g$ inferred in step 2 on our grid of model atmospheres and minimize the dependence of individual line-based iron abundance inferences on reduced equivalent width to derive model atmosphere $[\text{Fe}/\text{H}]_{\text{atmo}}$ and ξ values consistent with our measured Fe I & Fe II equivalent widths and our **isochrones** inferred T_{eff} & $\log g$.
4. We then use the model atmosphere selected in step 3 to calculate $[\text{Fe}/\text{H}]$ as the average of all $n_{\text{Fe}} = n_{\text{Fe I}} + n_{\text{Fe II}}$ equivalent width-based iron abundance inferences for individual Fe I & Fe II lines. We take the uncertainty of our $[\text{Fe}/\text{H}]$ inference as the standard deviation of the individual line-based abundance inferences $\sigma'_{[\text{Fe}/\text{H}]}$ divided by $\sqrt{n_{\text{Fe}}}$.

5. We next check if the $[\text{Fe}/\text{H}]$ inferred in step 4 agrees to two decimal places with $[\text{Fe}/\text{H}]_{\text{atmo}}$. If so, we proceed to step 6. If not, we replace $[\text{Fe}/\text{H}]_{\text{atmo}}$ with $[\text{Fe}/\text{H}]$ and repeat steps 3 to 5 until agreement is achieved.
6. We then repeat steps 2 to 5 until the metallicities inferred from both the **isochrones** analysis and the reduced equivalent width balance approach are consistent within their uncertainties (typically a few iterations).

We use a Monte Carlo simulation to derive the final values and uncertainties in our adopted $[\text{Fe}/\text{H}]$ and ξ values due to the uncertainties in our adopted T_{eff} and $\log g$.

1. We randomly sample a self-consistent pair of T_{eff} and $\log g$ from our converged **isochrones** posteriors described above and calculate the values of $[\text{Fe}/\text{H}]_{\text{atmo}}$ and ξ that produce the best reduced equivalent width balance given our Fe I & Fe II equivalent width measurements.
2. We use the model atmosphere selected in step 1 to calculate the average of all $n_{\text{Fe}} = n_{\text{Fe I}} + n_{\text{Fe II}}$ individual equivalent width-based iron abundance inferences and save the resulting metallicity of each iteration.
3. We repeat steps 1 and 2 200 times and adopt as our final photospheric stellar parameters the (16,50,84) percentiles of the 200 self-consistent sets of T_{eff} , $\log g$, $[\text{Fe}/\text{H}]$, and ξ produced in this way.

We find good agreement between these photospheric stellar parameter derived from our Monte Carlo simulation and those resulting from a single iteration of reduced equivalent width balance using the median T_{eff} and $\log g$ from the posteriors produced by our converged analysis. We report our adopted photospheric and fundamental stellar parameters in Table 1 and plot samples from their posteriors in Figure 1. All of the uncertainties quoted in Table 1 include random uncertainties only. That is, they are uncertainties derived under the unlikely assumption that the MIST isochrone grid we use in our analyses perfectly reproduces all stellar properties.

We use Transiting Exoplanet Survey Satellite (TESS - Ricker et al. 2015) data from Sectors 4 and 31 to measure the rotational period of WASP-77 A. We used the **eleanor** software framework⁷ (Feinstein et al. 2019)

⁴ <https://github.com/astroChasqui/q2>

⁵ <https://github.com/timothydmorton/isochrones>

⁶ <https://ccpforge.cse.rl.ac.uk/gf/project/multinest/>

⁷ <https://adina.feinste.in/eleanor/>

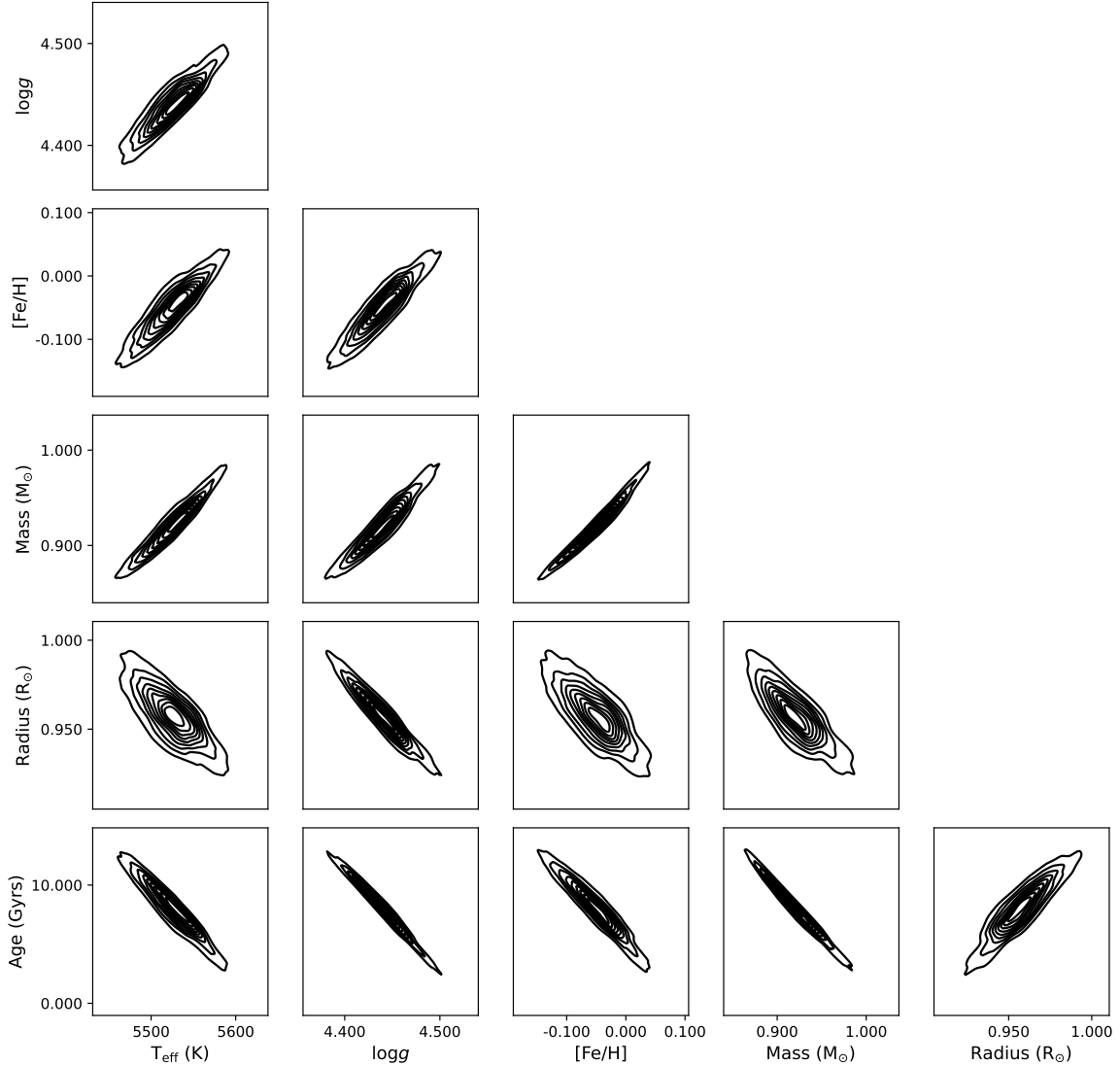


Figure 1. Samples from photospheric and fundamental stellar parameter posteriors from our Bayesian analyses of astrometric, photometric, and spectroscopic data for WASP-77 A. We emphasize that our adopted $[\text{Fe}/\text{H}]$ comes from averaging individual equivalent width-based iron abundance inferences as described above and not directly from the isochrones-inferred metallicity plotted here.

to generate light curves for WASP-77 A based on Sector 4 and 31 TESS full-frame image data. We masked data points coincident with transits of WASP-77 A b or that had non-zero data quality flags. We used the `lightkurve` package⁸ (Lightkurve Collaboration et al. 2018) to linearly flatten the light curves across a single-orbit window to preserve variability while removing orbit-to-orbit trends. After normalizing each light curve and eliminating 4σ outliers, we followed Healy & McCullough (2020) and Healy et al. (2021) to use both a stellar light curve’s autocorrelation function (ACF) and

its periodogram to infer stellar rotation period. For both the combined light curve and each sector individually, we used the first peak of the ACF and its half-width at half-maximum to estimate the rotation period of WASP-77 A and its uncertainty. In all cases, the ACFs indicate statistically consistent periods. The ACF-inferred rotation periods are consistent with the periodogram peaks for both the Sector 4 and the Sectors 4+31 analyses, though for the Sector 31 analysis the periodogram peak suggests a rotation period a factor of two higher than the ACF. Based on the combined two-sector light curve, the first peak of the ACF produces our final estimate of WASP-77 A’s rotation period $P_{\text{rot}} = 15.6 \pm 3.5$ reported in Table 1. The periodogram of the combined

⁸ <https://docs.lightkurve.org/>

Table 1. Adopted Stellar Parameters

Property	Value	Unit
SkyMapper DR2 u	12.084 ± 0.008	AB mag
SkyMapper DR2 v	11.756 ± 0.008	AB mag
SkyMapper DR2 g	10.443 ± 0.034	AB mag
SkyMapper DR2 r	10.088 ± 0.04	AB mag
SkyMapper DR2 z	9.881 ± 0.046	AB mag
Gaia DR2 DR2 G	10.096 ± 0.002	Vega mag
Gaia EDR3 parallax	9.459 ± 0.056	mas
Isochrone-inferred parameters		
Effective temperature T_{eff}	5525^{+23}_{-25}	K
Surface gravity $\log g$	4.44 ± 0.02	cm s^{-2}
Stellar mass M_*	0.92 ± 0.02	M_{\odot}
Stellar radius R_*	$0.96^{+0.01}_{-0.02}$	R_{\odot}
Luminosity L_*	0.77 ± 0.01	L_{\odot}
Isochrone-based age τ_{iso}	$7.99^{+1.90}_{-1.71}$	Gyr
Spectroscopically inferred parameters		
[Fe/H]	$-0.05^{+0.02}_{-0.01}$	
ξ	1.26 ± 0.02	km s^{-1}
Light-curve inferred parameters		
Rotational period P_{rot}	15.6 ± 3.5	day
Gyrochronology-based age τ_{gyro}	1.5	Gyr

two-sector light curve is consistent with this period determination. We use the the rotational evolution models presented in [van Saders et al. \(2016\)](#) to roughly infer an age $\tau_{\text{gyro}} \approx 1.5$ Gyr for WASP-77 A based on this rotation period inference.

To evaluate the impact any possible systematic uncertainties resulting from our analysis, we compare the photospheric and fundamental stellar parameters we infer for WASP-77 A with those reported by other groups for the same star. WASP-77 A was initially studied by [Maxted et al. \(2013\)](#) in the paper announcing the discovery of WASP-77 A b. Photospheric and/or fundamental parameters for the star based on high-resolution spectroscopy have since been published by [Mortier et al. \(2013\)](#) (updated in [Sousa et al. 2021](#)) and [Kolecki & Wang \(2021\)](#). [Maxted et al. \(2013\)](#) found $T_{\text{eff}} = 5500 \pm 80$ K, $\log g = 4.33 \pm 0.08$, $[\text{Fe}/\text{H}] = 0.00 \pm 0.11$, $M_* = 1.00 \pm 0.07 M_{\odot}$, $\tau_{\text{iso}} = 8$ Gyr, and $P_{\text{rot}} = 15.4 \pm 0.4$ days. [Mortier et al. \(2013\)](#) found $T_{\text{eff}} = 5605 \pm 41$ K, $\log g = 4.37 \pm 0.09$, $[\text{Fe}/\text{H}] = 0.07 \pm 0.03$, and $M_* = 0.96 \pm 0.07 M_{\odot}$. Updated parameters from the same group presented in [Sousa et al. \(2021\)](#) found $T_{\text{eff}} = 5595 \pm 16$ K, $\log g = 4.41 \pm 0.03$, $[\text{Fe}/\text{H}] = 0.01 \pm 0.01$, and $M_* = 0.915 \pm 0.004 M_{\odot}$.

[Kolecki & Wang \(2021\)](#) found $T_{\text{eff}} = 5660 \pm 30$ K, $\log g = 4.49 \pm 0.01$, and $[\text{Fe}/\text{H}] = -0.15 \pm 0.06$. Our photospheric and fundamental stellar parameters agree well with those presented in [Maxted et al. \(2013\)](#) and [Mortier et al. \(2013\)](#) as updated by [Sousa et al. \(2021\)](#). There is some tension between our parameters and those reported by [Kolecki & Wang \(2021\)](#) that we attribute to their neglect of extinction and their use of Two Micron All Sky Survey (2MASS) and Wide-field Infrared Survey Explorer (WISE) photometry for WASP-77 A that were contaminated by its binary companion WASP-77 B. The excellent agreement between our photospheric and fundamental stellar parameters for WASP-77 A and those inferred by other groups suggests that any systematic uncertainties present must be small.

As an additional check we inferred T_{eff} for WASP-77 A using the `colte` code⁹ ([Casagrande et al. 2021](#)) that estimates T_{eff} using a combination of color- T_{eff} relations obtained by implementing the InfraRed Flux Method for Gaia and 2MASS photometry. As required by `colte`, we used Gaia EDR3 G , G_{BP} , and G_{RP} plus 2MASS J , H , and K_s photometry as input. We used these data despite the fact that 2MASS J and H are affected by confusion and 2MASS K_s is affected by a diffraction spike. We find a `colte`-based $T_{\text{eff}} = 5354 \pm 203$ K. While we suspect its large uncertainty is due to the poor quality of the required input 2MASS photometry, it is consistent with our adopted $T_{\text{eff}} = 5525^{+23}_{-25}$ K.

There are significant differences between the ages inferred for WASP-77 A from isochrones and from gyrochronology. We find $\tau_{\text{iso}} = 7.99^{+1.90}_{-1.71}$ Gyr in full agreement with the $\tau_{\text{iso}} = 8$ Gyr inference from the full MCMC fit to all data from [Maxted et al. \(2013\)](#). These inferences are also consistent with the fits produced by five additional isochrones grids presented in [Maxted et al. \(2013\)](#) using the methodology described in [Southworth \(2012\)](#). Similarly, if we fit Yonsei-Yale isochrones ([Yi et al. 2001, 2003](#); [Kim et al. 2002](#); [Demarque et al. 2004](#)) to our T_{eff} and $\log g$ inferences using `q2` we find $\tau_{\text{iso}} = 8.3 \pm 3.5$ Gyr. On the other hand, [Maxted et al. \(2013\)](#) used their $P_{\text{rot}} = 15.4 \pm 0.4$ days to infer a gyrochronology-based age $\tau_{\text{gyro}} = 1.0^{+0.5}_{-0.3}$ Gyr using the gyrochronology relation from [Barnes \(2007\)](#). Using our TESS-based $P_{\text{rot}} = 15.6 \pm 3.5$ days we find $\tau_{\text{gyro}} \approx 1.5$ Gyr using the updated [van Saders et al. \(2016\)](#) models.

We argue that τ_{iso} should be preferred to τ_{gyro} for WASP-77 A. We assume that WASP-77 B has the same metallicity and extinction we inferred for WASP-77 A and use the same procedure described above to fit the

⁹ <https://github.com/casaluca/colte>

MIST isochrone grid to Sloan Digital Sky Survey (SDSS; Fukugita et al. 1996; Gunn et al. 1998, 2006; York et al. 2000; Doi et al. 2010; Abdurro’uf et al. 2021) u and Gaia DR2 G photometry as well as a Gaia EDR3 parallax for WASP-77 B. We find consistent ages for WASP-77 A $\tau_{\text{iso}} = 7.99^{+1.90}_{-1.71}$ and WASP-77 B $\tau_{\text{iso}} = 7.3^{+4.4}_{-4.6}$. We also note that Salz et al. (2015) studied the X-ray properties of the WASP-77 system and found X-ray-based ages consistent with our isochrone-based age inferences for both stars. As we will show in Section 6, the difference between the isochrone- and gyrochronology-based age inferences results from tidally mediated angular momentum exchange between the WASP-77 A system’s orbital angular momentum and the rotational angular momentum of WASP-77 A.

It has been proposed that the chemical abundances of solar neighborhood “solar twin” stars can be used as “chemical clocks” to complement other age inference techniques. WASP-77 A is a thin disk star, so its elemental abundances are the result of thin disk Galactic chemical evolution. We use our inferred elemental abundances and the empirical chemical clocks derived from thin disk solar twins by Spina et al. (2018) to infer two more, independent, age estimates based on $[\text{Y}/\text{Mg}]$ and $[\text{Y}/\text{Al}]$ abundance ratios. According to Equations (4) and (5) from Spina et al. (2018), WASP-77 A has a $[\text{Y}/\text{Mg}]$ chemical clock-based age $\tau_{\text{cc}} = 8.0 \pm 1.0$ Gyr and a $[\text{Y}/\text{Al}]$ chemical clock-based age $\tau_{\text{cc}} = 6.5 \pm 0.9$ Gyr. The consistency of τ_{iso} and these τ_{cc} estimates supports our interpretation of the gyrochronology-based age inferences for WASP-77 A.

4. ELEMENTAL ABUNDANCES

To infer the elemental abundances of several α , light odd- Z , iron-peak, and neutron-capture elements we first measure the equivalent widths of atomic absorption lines of C I, O I, Na I, Mg I, Al I, Si I, K I, Ca I, Sc II, Ti I, Ti II, V I, Cr I, Fe I, Fe II, Ni I, and Y II in our continuum-normalized spectrum by fitting Gaussian profiles with the `splot` task in IRAF. We use the `deblend` task to disentangle absorption lines from adjacent spectral features whenever necessary. We measure an equivalent width for every absorption line in our line list that could be recognized, taking into consideration the quality of the spectrum in the vicinity of a line and the availability of alternative transitions of the same species. We assume Asplund et al. (2021) solar abundances and local thermodynamic equilibrium (LTE) and use the 1D plane-parallel solar-composition ATLAS9 model atmospheres and the 2019 version of MOOG to infer elemental abundances based on each equivalent width measurement. We report our adopted atomic data, equivalent

width measurements, and individual line-based abundance inferences in Table 2.

We report in Table 3 our abundance inferences in three common systems: $A(\text{X})$, $[\text{X}/\text{H}]$, and $[\text{X}/\text{Fe}]$. The abundance $A(\text{X})$ is defined $A(\text{X}) = \log N_{\text{X}}/N_{\text{H}} + 12$, the abundance ratio $[\text{X}/\text{H}]$ is defined as $[\text{X}/\text{H}] = A(\text{X}) - A(\text{X})_{\odot}$, and the abundance ratio $[\text{X}/\text{Fe}]$ is defined as $[\text{X}/\text{Fe}] = [\text{X}/\text{H}] - [\text{Fe}/\text{H}]$. We define the uncertainty in the abundance ratio $\sigma_{[\text{X}/\text{H}]}$ as the standard deviation of the individual line-based abundance inferences $\sigma'_{[\text{X}/\text{H}]}$ divided by $\sqrt{n_{\text{X}}}$. We define the uncertainty $\sigma_{[\text{X}/\text{Fe}]}$ as the square root of the sum of squares of $\sigma_{[\text{X}/\text{H}]}$ and $\sigma_{[\text{Fe}/\text{H}]}$.

When possible, we update our elemental abundances derived under the assumptions of LTE to account for departures from LTE (i.e., non-LTE corrections) by linearly interpolating published grids of non-LTE corrections using `scipy` (Virtanen et al. 2020). We make use of 1D non-LTE corrections for carbon (Amarsi et al. 2020), oxygen (Amarsi et al. 2020), sodium (Lind et al. 2011), aluminum (Amarsi et al. 2020), silicon (Amarsi & Asplund 2017), potassium (Reggiani et al. 2019), calcium (Amarsi et al. 2020), and iron (Amarsi et al. 2016). We also make use of 3D non-LTE corrections for carbon and oxygen (Amarsi et al. 2019). We present these abundances corrected for departures from LTE in Table 3.

Our 1D non-LTE abundance corrections for carbon and oxygen come from Amarsi et al. (2020) and are limited to one carbon line and a mean correction for the three lines of the oxygen triplet. We therefore cannot calculate individual line-based abundance dispersions for our 1D non-LTE corrected carbon and oxygen abundance inferences, so our uncertainties might be underestimated. On the other hand, our 3D non-LTE carbon and oxygen abundance corrections come from Amarsi et al. (2019) and are available for all the lines in our line list. We do find good agreement between our 1D non-LTE and 3D non-LTE corrected carbon abundances for the one line with corrections in both sources. Because both our 1D non-LTE and 3D non-LTE corrected carbon and oxygen abundance inferences for WASP-77 A indicate that it has a sub-solar C/O ratio, our preference for 3D non-LTE corrected abundances does not affect the constraints we derive in Section 6 on the formation of WASP-77 A b.

Elemental abundances for WASP-77 A have also been published in Maxted et al. (2013) and Kolecki & Wang (2021). All of our elemental abundance inferences are consistent with those presented in Maxted et al. (2013).

Table 2. Atomic Data, Equivalent-width Measurements, and Individual-line Abundance Inferences

Wavelength (Å)	Species	Excitation Potential (eV)	$\log(gf)$	EW (mÅ)	$\log_\epsilon(X)$
6154.225	Na I	2.102	-1.547	47.8	6.302
6160.747	Na I	2.104	-1.246	59.4	6.169
4571.095	Mg I	0.000	-5.623	118.3	7.374
4730.040	Mg I	4.340	-2.389	71.6	7.595
6319.236	Mg I	5.108	-2.165	67.0	7.986
6318.717	Mg I	5.108	-1.945	54.4	7.603
6696.018	Al I	3.143	-1.481	49.4	6.453
6698.667	Al I	3.143	-1.782	28.3	6.391
7835.309	Al I	4.021	-0.680	46.7	6.371
7836.134	Al I	4.021	-0.450	66.1	6.376

NOTE—This table is published in its entirety in the machine-readable format. A portion is shown here for guidance regarding its form and content.

Our abundance inferences for carbon, sodium, magnesium, and silicon are consistent with those presented in Kolecki & Wang (2021), though our oxygen and potassium abundances are significantly higher than those presented in that paper. We are able to reproduce the oxygen abundance reported in Kolecki & Wang (2021) using their photospheric stellar parameters, our equivalent width measurements, and 3D non-LTE abundance corrections from Amarsi et al. (2019). We are therefore confident that the tension between our oxygen abundances results from the photospheric stellar parameters Kolecki & Wang (2021) derived for WASP-77 A that are hotter and more metal-poor than those derived by us, Maxted et al. (2013), and Mortier et al. (2013) as updated by Sousa et al. (2021).

5. UPDATED PLANETARY PARAMETERS

We make use of our accurate, precise, and self-consistent stellar mass and radius inferences for WASP-77 A to update the parameters of the planet WASP-77 A b. Taking the transit depth $\delta = (R_p/R_*)^2 = 0.01693 \pm 0.00017$ from Maxted et al. (2013), our stellar radius $R_* = 0.96^{+0.01}_{-0.02} R_\odot$ implies a planet radius $R_p = 0.125^{+0.001}_{-0.004} R_\odot = 1.22^{+0.01}_{-0.04} R_{\text{Jup}}$ in agreement with the $R_p = 1.21 \pm 0.02 R_{\text{Jup}}$ value inferred by Maxted et al. (2013). We fit the HARPS radial velocities from Maxted et al. (2013) as updated in Trifonov et al. (2020) using the RadVel package¹⁰ (Fulton et al. 2017, 2018). We fix the orbital period $P = 1.3600306 \pm 0.0000012$

days to the value from Turner et al. (2016). We fix the eccentricity $e = 0$ as expected for such a short-period hot Jupiter and find a planet mass $M_p = 1.66 \pm 0.03 M_{\text{Jup}}$, marginally lower than those presented in Maxted et al. (2013) and Bonomo et al. (2017). We plot our fit to the Doppler data in Figure 2 and summarize our updated planet parameters in Table 4.

6. DISCUSSION

6.1. The Atmospheric Abundances of WASP-77 A b Indicate it Formed Beyond the H₂O Ice Line

For the photosphere of WASP-77 A and therefore the protoplanetary disk in which WASP-77 A b formed, we find super-solar carbon and oxygen abundances with a sub-solar C/O abundance ratio¹¹. We infer $[C/H]_{3D \text{ non-LTE}} = 0.10 \pm 0.09$ and $[O/H]_{3D \text{ non-LTE}} = 0.23 \pm 0.02$, implying $[(C+O)/H]_{3D \text{ non-LTE}} = [A(C)_* - A(C)_\odot] + [A(O)_* - A(O)_\odot] = 0.33 \pm 0.09$ and C/O abundance ratios $[C/O]_{3D \text{ non-LTE}} = [C/H] - [O/H] = -0.13 \pm 0.09$ and $C/O_{3D \text{ non-LTE}} = 10^{A(C)-A(O)} = 0.44^{+0.07}_{-0.08}$.

For the atmosphere of the hot Jupiter WASP-77 A b, Line et al. (2021) found $[C/H] = -0.46^{+0.17}_{-0.16}$, $[O/H] = -0.49^{+0.14}_{-0.12}$, $[(C+O)/H] = -0.48^{+0.15}_{-0.13}$, and $C/O = 0.59 \pm 0.08$. Those authors also considered the possibility that cloud condensates like MgSiO₃ and Mg₂SiO₄ “rain out” on WASP-77 A b’s night side and

¹⁰ <https://radvel.readthedocs.io/en/latest/>

¹¹ According to Asplund et al. (2021), the solar C/O abundance ratio is $C/O = 0.59^{+0.08}_{-0.06}$.

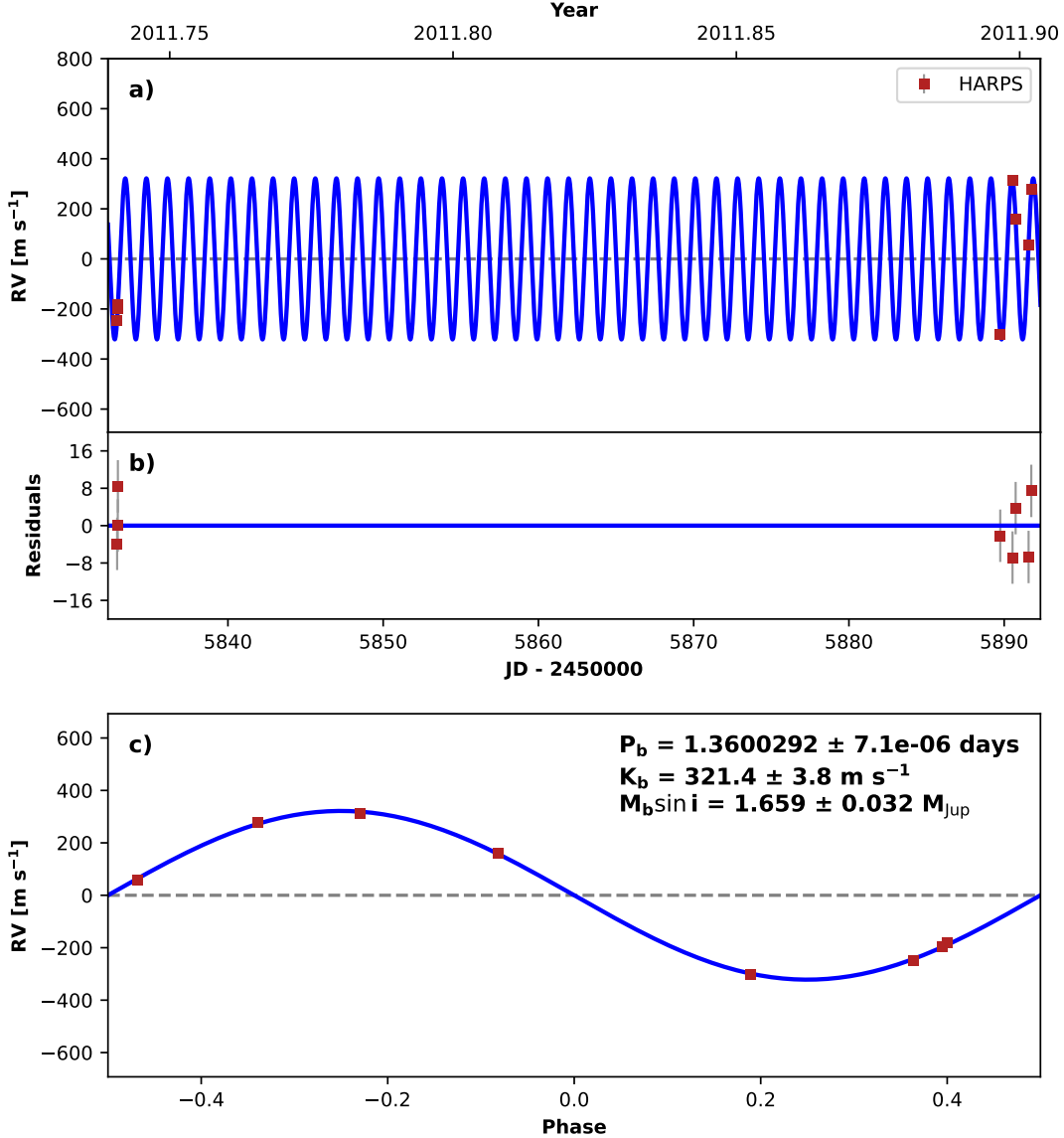


Figure 2. RadVel fit of a Keplerian orbit to the WASP-77 A differential radial velocities from [Maxted et al. \(2013\)](#) as updated in [Trifonov et al. \(2020\)](#). We fix the orbital period $P = 1.3600306 \pm 0.0000012$ to the value from [Turner et al. \(2016\)](#) and the eccentricity to zero as expected for short-period hot Jupiter orbiting a mature solar-type star. Using the stellar mass we inferred from our self-consistent analysis of astrometric, photometric, and spectroscopic data for WASP-77 A $M_* = 0.92 \pm 0.02 M_\odot$ we find that WASP-77 A b's mass is $M_p = 1.66 \pm 0.03 M_{\text{Jup}}$.

remove oxygen from its atmosphere. That process would enhance the gas-phase C/O ratio of WASP-77 A b. When accounting for this possibility, [Line et al. \(2021\)](#) found $[(\text{C}+\text{O})/\text{H}] = -0.41 \pm 0.14$ and $\text{C}/\text{O} = 0.46 \pm 0.08$ for the atmosphere of WASP-77 A b. [Line et al. \(2021\)](#) assumed that because of its near solar metallicity the star WASP-77 A has a solar C/O abundance ratio. Based on that assumption, those authors asserted that the atmosphere of the planet WASP-77 A b has sub-stellar $[\text{C}/\text{H}]$ and $[\text{O}/\text{H}]$ plus a stellar C/O abundance ratio. They suggested that WASP-77 A b accreted its

envelope interior to its parent protoplanetary disk's H₂O ice line from carbon-depleted gas with little subsequent planetesimal accretion or core erosion.

We find that carbon and oxygen are 3.6 times and 5.2 times less abundant in the atmosphere of WASP-77 A b than in the photosphere of WASP-77 A. Our abundance inferences for WASP-77 A increase the statistical significance of the [Line et al. \(2021\)](#) observation that WASP-77 A b's atmosphere has sub-stellar carbon and oxygen abundances, from 2.6 σ to 2.9 σ for carbon and from 3.4 σ to 5.1 σ for oxygen. Our C/O abundance ra-

Table 3. Elemental Abundances

Species	$A(X)$	$[X/H]$	$\sigma_{[X/H]}$	$[X/Fe]$	$\sigma_{[X/Fe]}$	n
LTE abundances						
C I	8.57	0.11	0.09	0.16	0.11	5
O I	9.03	0.34	0.02	0.39	0.04	3
Na I	6.24	0.02	0.05	0.07	0.07	2
Mg I	7.64	0.09	0.11	0.14	0.13	4
Al I	6.46	0.03	0.04	0.08	0.05	6
Si I	7.58	0.07	0.02	0.12	0.03	13
K I	5.20	0.13	...	0.18	0.06	1
Ca I	6.29	-0.01	0.03	0.04	0.05	11
Sc II	3.04	-0.11	0.03	-0.05	0.06	4
Ti I	4.92	-0.06	0.03	0.00	0.05	14
Ti II	5.00	0.03	0.04	0.08	0.06	10
V I	3.84	-0.06	0.03	-0.01	0.06	8
Cr I	5.51	-0.11	0.05	-0.06	0.06	10
Fe I	7.39	-0.07	0.01	80
Fe II	7.50	0.04	0.03	17
Ni I	6.23	0.03	0.02	0.08	0.03	17
Y II	2.14	-0.08	0.05	-0.02	0.08	5
1D non-LTE abundances						
C I	8.42	-0.04	...	-0.03	...	1
O I	8.93	0.24	...	0.25	...	3 ^a
Na I	6.16	-0.06	0.10	-0.05	0.10	2
Al I	6.35	-0.08	0.01	-0.07	0.01	2
Si I	7.56	0.05	0.03	0.06	0.03	13
K I	4.89	-0.18	...	-0.17	...	1
Ca I	6.07	-0.23	0.01	-0.22	0.01	2
Fe I	7.42	-0.04	0.01	80
Fe II	7.53	0.07	0.03	17
3D non-LTE abundances						
C I	8.56	0.10	0.09	0.15	0.09	5
O I	8.92	0.23	0.02	0.28	0.02	3
Additional abundance ratios of interest						
$[Fe/H]_{1D \text{ non-LTE}} = -0.01 \pm 0.01$						
$[(C+O)/H]_{3D \text{ non-LTE}} = 0.33 \pm 0.09$						
$[C/O]_{3D \text{ non-LTE}} = -0.13 \pm 0.09$						
$C/O_{3D \text{ non-LTE}} = 0.44^{+0.07}_{-0.08}$						

^a1D non-LTE corrections from Amarsi et al. (2020) for the three lines of the oxygen triplet are limited to a mean correction.

tio inference for WASP-77 A qualitatively changes the status of WASP-77 A b’s atmospheric C/O abundance ratio from stellar to super-stellar by a factor of 1.4 at the 1.4- σ level.

Table 4. Updated Planetary Parameters

Parameter	Credible Interval	Units
Fixed values		
Orbital period P_{orb}	1.3600306 ± 0.0000012	days
Eccentricity e	0.00	
Fit values		
Argument of periape ω	177 ± 120	degrees
Doppler semiamplitude K_*	$321.4^{+3.9}_{-3.8}$	m s^{-1}
Planet mass M_p	1.66 ± 0.03	M_{Jup}
Planet radius R_p	$1.22^{+0.01}_{-0.04}$	R_{Jup}
Planet density ρ_p	$1.14^{+0.12}_{-0.10}$	g cm^{-3}
Semimajor axis a	0.02338 ± 0.00017	AU

As we argued in Section 1, it is not trivial to connect a giant planet’s atmospheric carbon and oxygen abundances to its formation location in its parent protoplanetary disk. Nevertheless, WASP-77 A b’s significantly sub-stellar carbon and oxygen abundances combined with a super-stellar C/O abundance ratio is consistent with formation beyond its parent protoplanetary disk’s H₂O ice line (e.g., Öberg et al. 2011), possibly from pebble accretion followed by high-eccentricity migration after disk dissipation (e.g., Madhusudhan et al. 2014, 2017; Booth et al. 2017). The possibility that some of the oxygen in WASP-77 A b’s atmosphere has rained-out in the form of condensates means that the bulk C/O ratio of the planet may indeed match the stellar abundance.

The qualitative change in the interpretation of WASP-77 A b’s atmospheric carbon and oxygen abundances brought about by our inference of WASP-77 A’s non-solar [C/H], [O/H], and C/O abundance ratio emphasizes the importance of stellar abundance inferences for the interpretation of giant planet atmospheric abundances. Indeed, even though WASP-77 A has a solar metallicity $[Fe/H]_{1D \text{ non-LTE}} = -0.01 \pm 0.01$ it has non-solar carbon and oxygen abundances. To illustrate this point, we plot in Figure 3 the 1D non-LTE carbon and oxygen abundances of solar neighborhood dwarf stars (i.e., $\log g \geq 4$) over the 1D non-LTE correct metallicity range characteristic of virtually all known planet host stars $-0.5 \leq [Fe/H] \leq 0.5$ from the third data release of the Galactic Archaeology with HERMES (GALAH) survey (Buder et al. 2021). Figure 3 shows that WASP-77 A is fully consistent with the solar neighborhood carbon and oxygen abundance distributions. It also shows that the solar neighborhood carbon, oxygen, and C/O abundance ratios are much broader than usually considered

in planet formation models, with 95% of solar neighborhood dwarf stars in the ranges $-0.15 \leq [\text{C}/\text{Fe}] \leq 0.32$, $-0.19 \leq [\text{O}/\text{Fe}] \leq 0.43$, $-0.26 \leq [\text{C}/\text{O}] \leq 0.29$, and $0.27 \leq \text{C}/\text{O} \leq 0.94$.

If a planet host star's carbon and oxygen abundances are unknown, then a planet with a sub-stellar but super-solar C/O abundance ratio would be mischaracterized as carbon rich. Likewise, a planet with a super-stellar but sub-solar C/O abundance ratio would be mischaracterized as carbon poor. We therefore recommend that all future studies of exoplanet atmospheric abundances also infer stellar photospheric and fundamental parameters that are self-consistent and physically consistent with stellar evolution. Those photospheric stellar parameters should be used in all elemental abundance inferences, and those fundamental stellar parameters should be used to recalculate exoplanet parameters (e.g. M_p , R_p , $\log g_p$, etc) using observables like Doppler velocities and light curves. In that way, all of the parameters necessary to characterize an exoplanet system can be made self-consistent to eliminate the small but possibly important systematic uncertainties that can effect an exoplanet atmosphere abundance inference. If the photospheric stellar parameters that produce carbon and oxygen abundances are not used to self consistently infer (1) stellar masses and radii and (2) planet parameters using observables, then those photospheric abundances are not suitable for exoplanet atmospheric characterization (e.g., Kolecki & Wang 2021).

6.2. Angular Momentum Exchange Explains the Tension Between Isochrone- and Gyrochronology-based Ages for WASP-77 A

The utility of gyrochronology-based age inferences for hot Jupiter host stars has been questioned both theoretically and empirically (e.g., Barnes 2007; Brown 2014; Tejada Arevalo et al. 2021). Similarly, we argue that gyrochronology-based age inferences for WASP-77 A are unreliable because of the possibility of tidally mediated angular momentum exchange between the system's orbital angular momentum L_{orb} and the rotational angular momentum of the host star WASP-77 A L_{rot} (the rotational angular momentum of WASP-77 A b is negligible). The total angular momentum L_{tot} of the WASP-77 A system in its current configuration is

$$L_{\text{tot},2} = L_{\text{orb},2} + L_{\text{rot},2}, \quad (1)$$

$$L_{\text{orb},2} = \left(\frac{M_* M_p}{M_* + M_p} \right) \left(\frac{2\pi}{P_{\text{orb},2}} \right) a_2^2 \sqrt{1 - e^2}, \quad (2)$$

$$L_{\text{rot},2} = I_* P_{\text{rot},2}. \quad (3)$$

Given the currently observed stellar rotation period $P_{\text{rot},2} = 15.6 \pm 3.5$ days, the system's orbital period

$P_{\text{orb},2} = 1.3600306 \pm 0.0000012$ days, and the system's semimajor axis $a_2 = 0.0234 \pm 0.0002$ AU, if we assume a constant stellar moment of inertia I_* with the solar value $I/(M_\odot R_\odot^2) = 0.070$, the stellar mass and radius we inferred $M_* = 0.92 \pm 0.02 M_\odot$ and $R_* = 0.96_{-0.02}^{+0.01} R_\odot$, and the planet mass we inferred $M_p = 1.66 \pm 0.03 M_{\text{Jup}}$, we find $L_{\text{orb},2} = 2.05 \times 10^{49} \text{ g cm}^2 \text{ s}^{-1}$, $L_{\text{rot},2} = 3.2 \times 10^{48} \text{ g cm}^2 \text{ s}^{-1}$, and $L_{\text{tot},2} = 2.4 \times 10^{49} \text{ g cm}^2 \text{ s}^{-1}$.

For our isochrone-inferred age of the system $\tau_{\text{iso}} = 7.99_{-1.71}^{+1.90}$ Gyr, the rotational evolution models of van Saders et al. (2016) predict $P_{\text{rot}} \approx 30$ days for a system with the zero-age main sequence T_{eff} expected for WASP-77 A. Assuming the conservation of angular momentum over the system's evolution and taking $P_{\text{rot},1} \approx 30$ days as the rotation period WASP-77 A would have had in the absence of tidal evolution, we find that the current rapid rotation of WASP-77 A given the system's age can be explained if the system had $P_{\text{orb},1} \approx 1.7$ days and $a_1 \approx 0.027$ AU before tidal evolution. That is, the disagreement between the isochrone- and gyrochronology-based ages for WASP-77 A can easily be explained by tidal evolution mediated angular momentum exchange.

Making the assumptions that the orbit of the WASP-77 A system had circularized early in its evolution and that the spin-up of WASP-77 A results from tidally mediated angular momentum exchange after orbit circularization, one can analytically solve the ordinary differential equation for semimajor axis evolution from Jackson et al. (2008) for WASP-77 A's tidal dissipation parameter Q'_* (i.e., following the convention of Goldreich & Soter 1966). Taking $a_1 \approx 0.027$ AU, $a_2 \approx 0.023$ AU, and $\Delta t \approx 8$ Gyr we find $Q'_* \sim 10^8$. In other words, even in the limit of inefficient dissipation tides can easily explain the spin-up of WASP-77 A due to tidal evolution over the life of the system. These results provide further evidence that gyrochronology-based ages should not be relied on for hot Jupiter systems.

7. CONCLUSION

We find that the hot Jupiter host star WASP-77 A has super-solar carbon $[\text{C}/\text{H}]_{3\text{D non-LTE}} = 0.10 \pm 0.09$ and oxygen $[\text{O}/\text{H}]_{3\text{D non-LTE}} = 0.23 \pm 0.02$ abundances plus sub-solar C/O abundance ratios $[\text{C}/\text{O}]_{3\text{D non-LTE}} = -0.13 \pm 0.09$ and $\text{C}/\text{O}_{3\text{D non-LTE}} = 0.44_{-0.08}^{+0.07}$. As reported by Line et al. (2021), the atmosphere of the hot Jupiter WASP-77 A b has $[\text{C}/\text{H}] = -0.46_{-0.16}^{+0.17}$, $[\text{O}/\text{H}] = -0.49_{-0.12}^{+0.14}$, and $\text{C}/\text{O} = 0.59 \pm 0.08$. Though Line et al. (2021) assumed that WASP-77 A has solar carbon and oxygen abundances and therefore asserted that WASP-77 A b has a stellar C/O abundance ratio, we find that WASP-77 A b has a significantly super-

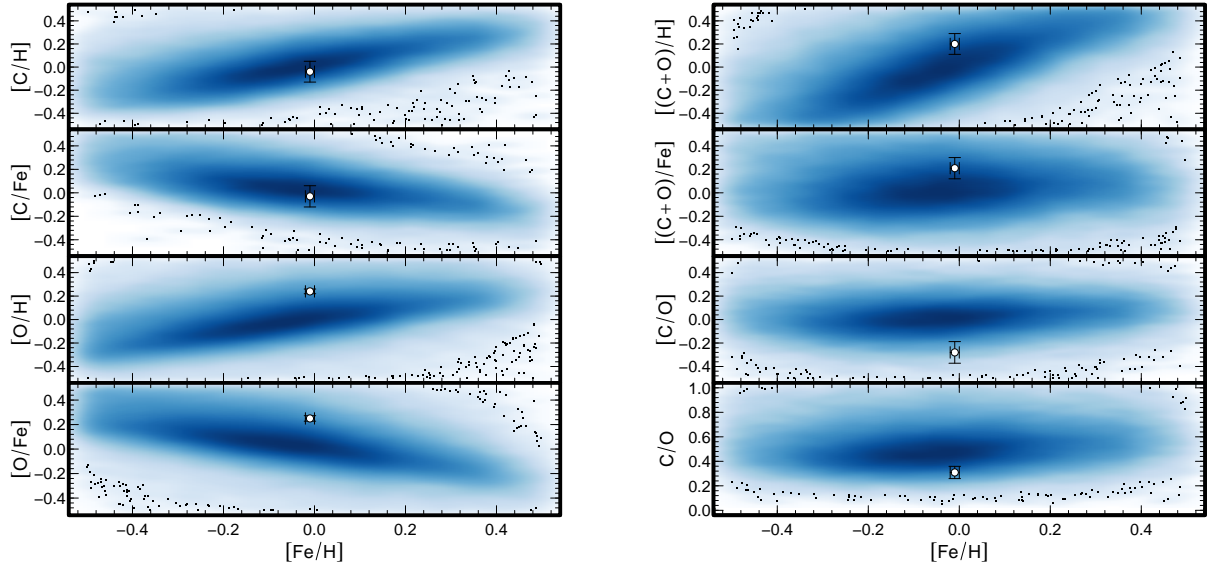


Figure 3. 1D non-LTE carbon and oxygen abundances of WASP-77 A compared to the same 1D non-LTE abundances for solar neighborhood dwarfs from GALAH DR3 (Buder et al. 2021). In each kernel density estimator-smoothed scatter plot, darker blue regions correspond to more densely populated regions of abundance space. We plot outliers as individual dots. We plot our abundance inferences for WASP-77 A’s as black-bordered white points. Left: $[C/H]$, $[C/Fe]$, $[O/H]$, and $[O/Fe]$. Right: $[(C+O)/H]$, $[(C+O)/Fe]$, $[C/O]$, and C/O . In the range $-0.1 \leq [Fe/H] \leq 0$, WASP-77 A is consistent with the GALAH-inferred carbon ($[C/Fe] = 0.05^{+0.12}_{-0.10}$), oxygen ($[O/Fe] = 0.06^{+0.14}_{-0.10}$), and C/O abundance ratio distributions ($[C/O] = 0.01^{+0.11}_{-0.12}$ and $C/O = 0.49^{+0.15}_{-0.12}$). In the metallicity range $-0.5 \leq [Fe/H] \leq 0.5$ appropriate for virtually all known exoplanet host stars, GALAH DR3 finds that 95% of solar neighborhood dwarf stars have $-0.15 \leq [C/Fe] \leq 0.32$, $-0.19 \leq [O/Fe] \leq 0.43$, $-0.26 \leq [C/O] \leq 0.29$, and $0.27 \leq C/O \leq 0.94$. These broad distributions emphasize that the assumption of solar abundance ratios of carbon and oxygen for exoplanet host stars is not always appropriate.

stellar C/O abundance ratio. The non-solar abundance ratios of WASP-77 A qualitatively change the interpretation of WASP-77 A b’s atmospheric abundances put forward in Line et al. (2021). While Line et al. (2021) suggested that WASP-77 A b formed its envelope interior to its parent protoplanetary disk’s H_2O ice line from carbon-depleted gas with little subsequent planetesimal accretion or core erosion, we find that its super-stellar C/O abundance ratio implies formation outside its parent protoplanetary disk’s H_2O ice line.

While the use of exoplanet atmospheric abundances to inform planet formation is not always straightforward, this qualitative change in the interpretation of the atmospheric abundances of WASP-77 A b emphasizes the importance of exoplanet host star elemental abundances inferences. For the most powerful constraints, these carbon and oxygen abundances cannot be inferred independently of stellar and exoplanet parameters. Instead, photospheric and fundamental stellar parameters that are self-consistent and physically consistent with stellar evolution should be used both in elemental abundance inferences and to re-derive planet parameters from observables like Doppler velocities and light curves. This approach results in self-consistent photospheric and fundamental stellar parameters, elemental abundances, and

exoplanet parameters that can be used to explore planet formation and evolution. Accounting for the possibility of tidally mediated angular momentum exchange in the WASP-77 A system resolves the tension between its isochrone- and gyrochronology-based ages. This result is further evidence that in general gyrochronology-based ages should not be relied on for hot Jupiter systems.

We thank the referee for a prompt and helpful review. Henrique Reggiani acknowledges support from a Carnegie Fellowship. Based on observations obtained with the Apache Point Observatory 3.5-meter telescope, which is owned and operated by the Astrophysical Research Consortium. The national facility capability for SkyMapper has been funded through ARC LIEF grant LE130100104 from the Australian Research Council, awarded to the University of Sydney, the Australian National University, Swinburne University of Technology, the University of Queensland, the University of Western Australia, the University of Melbourne, Curtin University of Technology, Monash University and the Australian Astronomical Observatory. SkyMapper is owned and operated by The Australian National University's Research School of Astronomy and Astrophysics. The survey data were processed and provided by the SkyMapper Team at ANU. The SkyMapper node of the All-Sky Virtual Observatory (ASVO) is hosted at the National Computational Infrastructure (NCI). Development and support of the SkyMapper node of the ASVO has been funded in part by Astronomy Australia Limited (AAL) and the Australian Government through the Commonwealth's Education Investment Fund (EIF) and National Collaborative Research Infrastructure Strategy (NCRIS), particularly the National eResearch Collaboration Tools and Resources (NeCTAR) and the Australian National Data Service Projects (ANDS). This work has made use of data from the European Space Agency (ESA) mission *Gaia* (<https://www.cosmos.esa.int/gaia>), processed by the *Gaia* Data Processing and Analysis Consortium (DPAC, <https://www.cosmos.esa.int/web/gaia/dpac/consortium>). Funding for the DPAC has been provided by national institutions, in particular the institutions participating in the *Gaia* Multilateral Agreement. This publication makes use of data products from the Two Micron All Sky Survey, which is a joint project of the University of Massachusetts and the Infrared Processing and Analysis Center/California Institute of Technology, funded by the National Aeronautics and Space Administration and the National Science Foundation. This research has made use of the NASA/IPAC Infrared Science Archive, which is funded by the National Aeronautics and Space Administration and operated by the California Institute of Technology. Funding for the Sloan Digital Sky Survey IV has been provided by the Alfred P. Sloan Foundation, the U.S. Department of Energy Office of Science, and the Participating Institutions. SDSS-IV acknowledges support and resources from the Center for High Performance Computing at the University of Utah. The SDSS website is www.sdss.org. SDSS-IV is managed by the Astrophysical Research Consortium for the Participating Institutions of the SDSS Collaboration including the Brazilian Participation Group, the Carnegie Institution for Science, Carnegie Mellon University, Center for Astrophysics, Harvard & Smithsonian, the Chilean Partici-

Facilities: ARC, CDS, Exoplanet Archive, Gaia, IRSA, SkyMapper, Sloan, TESS

Software: `astropy` (Astropy Collaboration et al. 2013, 2018), `CERES` (Brahm et al. 2017), `colte` (Casagrande et al. 2021), `eleanor` (Feinstein et al. 2019), `IRAF` (Tody 1986, 1993), `isochrones` (Morton 2015), `iSpec` (Blanco-Cuaresma et al. 2014; Blanco-Cuaresma 2019), `lightkurve` (Lightkurve Collaboration et al. 2018), `MOOG` (Snedden 1973), `MultiNest` (Feroz & Hobson 2008; Feroz et al. 2009, 2019), `numpy` (Harris et al. 2020), `pandas` (McKinney 2010; pandas Development Team 2020), `PyMultiNest` (Buchner et al. 2014), `q2` (Ramírez et al. 2014), `RadVel` (Fulton et al. 2017, 2018), `scipy` (Virtanen et al. 2020)

REFERENCES

- Abdurro'uf, Accetta, K., Aerts, C., et al. 2021, arXiv e-prints, arXiv:2112.02026.
<https://arxiv.org/abs/2112.02026>
- Ali-Dib, M. 2017, MNRAS, 467, 2845,
 doi: [10.1093/mnras/stx260](https://doi.org/10.1093/mnras/stx260)
- Ali-Dib, M., Mousis, O., Petit, J.-M., & Lunine, J. I. 2014, ApJ, 785, 125, doi: [10.1088/0004-637X/785/2/125](https://doi.org/10.1088/0004-637X/785/2/125)
- Amarsi, A. M., & Asplund, M. 2017, MNRAS, 464, 264,
 doi: [10.1093/mnras/stw2445](https://doi.org/10.1093/mnras/stw2445)
- Amarsi, A. M., Lind, K., Asplund, M., Barklem, P. S., & Collet, R. 2016, MNRAS, 463, 1518,
 doi: [10.1093/mnras/stw2077](https://doi.org/10.1093/mnras/stw2077)
- Amarsi, A. M., Nissen, P. E., & Skúladóttir, Á. 2019, A&A, 630, A104, doi: [10.1051/0004-6361/201936265](https://doi.org/10.1051/0004-6361/201936265)
- Amarsi, A. M., Lind, K., Osorio, Y., et al. 2020, A&A, 642, A62, doi: [10.1051/0004-6361/202038650](https://doi.org/10.1051/0004-6361/202038650)
- Arenou, F., Luri, X., Babusiaux, C., et al. 2018, A&A, 616, A17, doi: [10.1051/0004-6361/201833234](https://doi.org/10.1051/0004-6361/201833234)
- Asplund, M., Amarsi, A. M., & Grevesse, N. 2021, A&A, 653, A141, doi: [10.1051/0004-6361/202140445](https://doi.org/10.1051/0004-6361/202140445)
- Astropy Collaboration, Robitaille, T. P., Tollerud, E. J., et al. 2013, A&A, 558, A33,
 doi: [10.1051/0004-6361/201322068](https://doi.org/10.1051/0004-6361/201322068)
- Astropy Collaboration, Price-Whelan, A. M., Sipőcz, B. M., et al. 2018, AJ, 156, 123, doi: [10.3847/1538-3881/aabc4f](https://doi.org/10.3847/1538-3881/aabc4f)
- Barnes, S. A. 2007, ApJ, 669, 1167, doi: [10.1086/519295](https://doi.org/10.1086/519295)
- Blanco-Cuaresma, S. 2019, MNRAS, 486, 2075,
 doi: [10.1093/mnras/stz549](https://doi.org/10.1093/mnras/stz549)
- Blanco-Cuaresma, S., Soubiran, C., Heiter, U., & Jofré, P. 2014, A&A, 569, A111,
 doi: [10.1051/0004-6361/201423945](https://doi.org/10.1051/0004-6361/201423945)
- Bonomo, A. S., Desidera, S., Benatti, S., et al. 2017, A&A, 602, A107, doi: [10.1051/0004-6361/201629882](https://doi.org/10.1051/0004-6361/201629882)
- Booth, R. A., Clarke, C. J., Madhusudhan, N., & Ilee, J. D. 2017, MNRAS, 469, 3994, doi: [10.1093/mnras/stx1103](https://doi.org/10.1093/mnras/stx1103)
- Brahm, R., Jordán, A., & Espinoza, N. 2017, PASP, 129, 034002, doi: [10.1088/1538-3873/aa5455](https://doi.org/10.1088/1538-3873/aa5455)
- Brown, D. J. A. 2014, MNRAS, 442, 1844,
 doi: [10.1093/mnras/stu950](https://doi.org/10.1093/mnras/stu950)
- Buchner, J., Georgakakis, A., Nandra, K., et al. 2014, A&A, 564, A125, doi: [10.1051/0004-6361/201322971](https://doi.org/10.1051/0004-6361/201322971)
- Buder, S., Sharma, S., Kos, J., et al. 2021, MNRAS, 506, 150, doi: [10.1093/mnras/stab1242](https://doi.org/10.1093/mnras/stab1242)
- Capitaniao, L., Lallement, R., Vergely, J. L., Elyajouri, M., & Monreal-Ibero, A. 2017, A&A, 606, A65,
 doi: [10.1051/0004-6361/201730831](https://doi.org/10.1051/0004-6361/201730831)
- Casagrande, L., Lin, J., Rains, A. D., et al. 2021, MNRAS, 507, 2684, doi: [10.1093/mnras/stab2304](https://doi.org/10.1093/mnras/stab2304)
- Castelli, F., & Kurucz, R. L. 2003, in Modelling of Stellar Atmospheres, ed. N. Piskunov, W. W. Weiss, & D. F. Gray, Vol. 210, A20.
<https://arxiv.org/abs/astro-ph/0405087>
- Choi, J., Dotter, A., Conroy, C., et al. 2016, ApJ, 823, 102,
 doi: [10.3847/0004-637X/823/2/102](https://doi.org/10.3847/0004-637X/823/2/102)
- Cridland, A. J., Eistrup, C., & van Dishoeck, E. F. 2019a, A&A, 627, A127, doi: [10.1051/0004-6361/201834378](https://doi.org/10.1051/0004-6361/201834378)
- Cridland, A. J., Pudritz, R. E., & Alessi, M. 2016, MNRAS, 461, 3274, doi: [10.1093/mnras/stw1511](https://doi.org/10.1093/mnras/stw1511)
- Cridland, A. J., van Dishoeck, E. F., Alessi, M., & Pudritz, R. E. 2019b, A&A, 632, A63,
 doi: [10.1051/0004-6361/201936105](https://doi.org/10.1051/0004-6361/201936105)
- . 2020, A&A, 642, A229,
 doi: [10.1051/0004-6361/202038767](https://doi.org/10.1051/0004-6361/202038767)
- Demarque, P., Woo, J.-H., Kim, Y.-C., & Yi, S. K. 2004, ApJS, 155, 667, doi: [10.1086/424966](https://doi.org/10.1086/424966)
- Doi, M., Tanaka, M., Fukugita, M., et al. 2010, AJ, 139, 1628, doi: [10.1088/0004-6256/139/4/1628](https://doi.org/10.1088/0004-6256/139/4/1628)
- Dotter, A. 2016, ApJS, 222, 8,
 doi: [10.3847/0067-0049/222/1/8](https://doi.org/10.3847/0067-0049/222/1/8)
- Eistrup, C., Walsh, C., & van Dishoeck, E. F. 2018, A&A, 613, A14, doi: [10.1051/0004-6361/201731302](https://doi.org/10.1051/0004-6361/201731302)
- Evans, D. W., Riello, M., De Angeli, F., et al. 2018, A&A, 616, A4, doi: [10.1051/0004-6361/201832756](https://doi.org/10.1051/0004-6361/201832756)
- Fabrizius, C., Luri, X., Arenou, F., et al. 2021, A&A, 649, A5, doi: [10.1051/0004-6361/202039834](https://doi.org/10.1051/0004-6361/202039834)
- Feinstein, A. D., Montet, B. T., Foreman-Mackey, D., et al. 2019, PASP, 131, 094502, doi: [10.1088/1538-3873/ab291c](https://doi.org/10.1088/1538-3873/ab291c)
- Feroz, F., & Hobson, M. P. 2008, MNRAS, 384, 449,
 doi: [10.1111/j.1365-2966.2007.12353.x](https://doi.org/10.1111/j.1365-2966.2007.12353.x)
- Feroz, F., Hobson, M. P., & Bridges, M. 2009, MNRAS, 398, 1601, doi: [10.1111/j.1365-2966.2009.14548.x](https://doi.org/10.1111/j.1365-2966.2009.14548.x)
- Feroz, F., Hobson, M. P., Cameron, E., & Pettitt, A. N. 2019, The Open Journal of Astrophysics, 2, 10,
 doi: [10.21105/astro.1306.2144](https://doi.org/10.21105/astro.1306.2144)
- Fukugita, M., Ichikawa, T., Gunn, J. E., et al. 1996, AJ, 111, 1748, doi: [10.1086/117915](https://doi.org/10.1086/117915)
- Fulton, B. J., Petigura, E. A., Blunt, S., & Sinukoff, E. 2017, RadVel: The Radial Velocity Fitting Toolkit,
 doi: [10.5281/zenodo.580821](https://doi.org/10.5281/zenodo.580821)
- . 2018, PASP, 130, 044504,
 doi: [10.1088/1538-3873/aaaaa8](https://doi.org/10.1088/1538-3873/aaaaa8)
- Gaia Collaboration, Prusti, T., de Bruijne, J. H. J., et al. 2016, A&A, 595, A1, doi: [10.1051/0004-6361/201629272](https://doi.org/10.1051/0004-6361/201629272)
- Gaia Collaboration, Brown, A. G. A., Vallenari, A., et al. 2018, A&A, 616, A1, doi: [10.1051/0004-6361/201833051](https://doi.org/10.1051/0004-6361/201833051)
- . 2021, A&A, 649, A1, doi: [10.1051/0004-6361/202039657](https://doi.org/10.1051/0004-6361/202039657)

- Goldreich, P., & Soter, S. 1966, *Icarus*, 5, 375, doi: [10.1016/0019-1035\(66\)90051-0](https://doi.org/10.1016/0019-1035(66)90051-0)
- Gunn, J. E., Carr, M., Rockosi, C., et al. 1998, *AJ*, 116, 3040, doi: [10.1086/300645](https://doi.org/10.1086/300645)
- Gunn, J. E., Siegmund, W. A., Mannery, E. J., et al. 2006, *AJ*, 131, 2332, doi: [10.1086/500975](https://doi.org/10.1086/500975)
- Hambly, N. C., Cropper, M., Boudreault, S., et al. 2018, *A&A*, 616, A15, doi: [10.1051/0004-6361/201832716](https://doi.org/10.1051/0004-6361/201832716)
- Harris, C. R., Millman, K. J., van der Walt, S. J., et al. 2020, *Nature*, 585, 357, doi: [10.1038/s41586-020-2649-2](https://doi.org/10.1038/s41586-020-2649-2)
- Harsono, D., Bruderer, S., & van Dishoeck, E. F. 2015, *A&A*, 582, A41, doi: [10.1051/0004-6361/201525966](https://doi.org/10.1051/0004-6361/201525966)
- Healy, B. F., & McCullough, P. R. 2020, *ApJ*, 903, 99, doi: [10.3847/1538-4357/abbc03](https://doi.org/10.3847/1538-4357/abbc03)
- Healy, B. F., McCullough, P. R., & Schlaufman, K. C. 2021, *ApJ*, 923, 23, doi: [10.3847/1538-4357/ac281d](https://doi.org/10.3847/1538-4357/ac281d)
- Jackson, B., Greenberg, R., & Barnes, R. 2008, *ApJ*, 678, 1396, doi: [10.1086/529187](https://doi.org/10.1086/529187)
- Kim, Y.-C., Demarque, P., Yi, S. K., & Alexander, D. R. 2002, *ApJS*, 143, 499, doi: [10.1086/343041](https://doi.org/10.1086/343041)
- Kolecki, J. R., & Wang, J. 2021, arXiv e-prints, arXiv:2112.02031. <https://arxiv.org/abs/2112.02031>
- Lallement, R., Vergely, J. L., Valette, B., et al. 2014, *A&A*, 561, A91, doi: [10.1051/0004-6361/201322032](https://doi.org/10.1051/0004-6361/201322032)
- Lallement, R., Capitano, L., Ruiz-Dern, L., et al. 2018, *A&A*, 616, A132, doi: [10.1051/0004-6361/201832832](https://doi.org/10.1051/0004-6361/201832832)
- Leconte, J., & Chabrier, G. 2012, *A&A*, 540, A20, doi: [10.1051/0004-6361/201117595](https://doi.org/10.1051/0004-6361/201117595)
- Lightkurve Collaboration, Cardoso, J. V. d. M., Hedges, C., et al. 2018, Lightkurve: Kepler and TESS time series analysis in Python. <http://ascl.net/1812.013>
- Lind, K., Asplund, M., Barklem, P. S., & Belyaev, A. K. 2011, *A&A*, 528, A103, doi: [10.1051/0004-6361/201016095](https://doi.org/10.1051/0004-6361/201016095)
- Lindgren, L., Bastian, U., Biermann, M., et al. 2021a, *A&A*, 649, A4, doi: [10.1051/0004-6361/202039653](https://doi.org/10.1051/0004-6361/202039653)
- Lindgren, L., Klioner, S. A., Hernández, J., et al. 2021b, *A&A*, 649, A2, doi: [10.1051/0004-6361/202039709](https://doi.org/10.1051/0004-6361/202039709)
- Line, M. R., Brogi, M., Bean, J. L., et al. 2021, *Nature*, 598, 580, doi: [10.1038/s41586-021-03912-6](https://doi.org/10.1038/s41586-021-03912-6)
- Lothringer, J. D., Rustamkulov, Z., Sing, D. K., et al. 2021, *ApJ*, 914, 12, doi: [10.3847/1538-4357/abf8a9](https://doi.org/10.3847/1538-4357/abf8a9)
- Madhusudhan, N., Amin, M. A., & Kennedy, G. M. 2014, *ApJL*, 794, L12, doi: [10.1088/2041-8205/794/1/L12](https://doi.org/10.1088/2041-8205/794/1/L12)
- Madhusudhan, N., Bitsch, B., Johansen, A., & Eriksson, L. 2017, *MNRAS*, 469, 4102, doi: [10.1093/mnras/stx1139](https://doi.org/10.1093/mnras/stx1139)
- Maxted, P. F. L., Anderson, D. R., Collier Cameron, A., et al. 2013, *PASP*, 125, 48, doi: [10.1086/669231](https://doi.org/10.1086/669231)
- McKinney, W. 2010, in Proceedings of the 9th Python in Science Conference, ed. Stéfan van der Walt & Jarrod Millman, 56 – 61, doi: [10.25080/Majora-92bf1922-00a](https://doi.org/10.25080/Majora-92bf1922-00a)
- Meléndez, J., Schirbel, L., Monroe, T. R., et al. 2014, *A&A*, 567, L3, doi: [10.1051/0004-6361/201424172](https://doi.org/10.1051/0004-6361/201424172)
- Mordasini, C., Klahr, H., Alibert, Y., Miller, N., & Henning, T. 2014, *A&A*, 566, A141, doi: [10.1051/0004-6361/201321479](https://doi.org/10.1051/0004-6361/201321479)
- Mordasini, C., van Boekel, R., Mollière, P., Henning, T., & Benneke, B. 2016, *ApJ*, 832, 41, doi: [10.3847/0004-637X/832/1/41](https://doi.org/10.3847/0004-637X/832/1/41)
- Mortier, A., Santos, N. C., Sousa, S. G., et al. 2013, *A&A*, 558, A106, doi: [10.1051/0004-6361/201322240](https://doi.org/10.1051/0004-6361/201322240)
- Morton, T. D. 2015, isochrones: Stellar model grid package. <http://ascl.net/1503.010>
- Notsu, S., Eistrup, C., Walsh, C., & Nomura, H. 2020, *MNRAS*, 499, 2229, doi: [10.1093/mnras/staa2944](https://doi.org/10.1093/mnras/staa2944)
- Öberg, K. I., Murray-Clay, R., & Bergin, E. A. 2011, *ApJL*, 743, L16, doi: [10.1088/2041-8205/743/1/L16](https://doi.org/10.1088/2041-8205/743/1/L16)
- Ochsenbein, F., Bauer, P., & Marcout, J. 2000, *A&AS*, 143, 23, doi: [10.1051/aas:2000169](https://doi.org/10.1051/aas:2000169)
- Onken, C. A., Wolf, C., Bessell, M. S., et al. 2019, *PASA*, 36, e033, doi: [10.1017/pasa.2019.27](https://doi.org/10.1017/pasa.2019.27)
- pandas Development Team. 2020, pandas-dev/pandas: Pandas, latest, Zenodo, doi: [10.5281/zenodo.3509134](https://doi.org/10.5281/zenodo.3509134)
- Paxton, B., Bildsten, L., Dotter, A., et al. 2011, *ApJS*, 192, 3, doi: [10.1088/0067-0049/192/1/3](https://doi.org/10.1088/0067-0049/192/1/3)
- Paxton, B., Cantiello, M., Arras, P., et al. 2013, *ApJS*, 208, 4, doi: [10.1088/0067-0049/208/1/4](https://doi.org/10.1088/0067-0049/208/1/4)
- Paxton, B., Marchant, P., Schwab, J., et al. 2015, *ApJS*, 220, 15, doi: [10.1088/0067-0049/220/1/15](https://doi.org/10.1088/0067-0049/220/1/15)
- Paxton, B., Schwab, J., Bauer, E. B., et al. 2018, *ApJS*, 234, 34, doi: [10.3847/1538-4365/aaa5a8](https://doi.org/10.3847/1538-4365/aaa5a8)
- Paxton, B., Smolec, R., Schwab, J., et al. 2019, *ApJS*, 243, 10, doi: [10.3847/1538-4365/ab2241](https://doi.org/10.3847/1538-4365/ab2241)
- Piso, A.-M. A., Öberg, K. I., Birnstiel, T., & Murray-Clay, R. A. 2015, *ApJ*, 815, 109, doi: [10.1088/0004-637X/815/2/109](https://doi.org/10.1088/0004-637X/815/2/109)
- Ramírez, I., Meléndez, J., Bean, J., et al. 2014, *A&A*, 572, A48, doi: [10.1051/0004-6361/201424244](https://doi.org/10.1051/0004-6361/201424244)
- Reggiani, H., Schlaufman, K. C., Casey, A. R., & Ji, A. P. 2020, *AJ*, 160, 173, doi: [10.3847/1538-3881/aba948](https://doi.org/10.3847/1538-3881/aba948)
- Reggiani, H., Schlaufman, K. C., Casey, A. R., Simon, J. D., & Ji, A. P. 2021, *AJ*, 162, 229, doi: [10.3847/1538-3881/ac1f9a](https://doi.org/10.3847/1538-3881/ac1f9a)
- Reggiani, H., Amarsi, A. M., Lind, K., et al. 2019, *A&A*, 627, A177, doi: [10.1051/0004-6361/201935156](https://doi.org/10.1051/0004-6361/201935156)
- Ricker, G. R., Winn, J. N., Vanderspek, R., et al. 2015, *Journal of Astronomical Telescopes, Instruments, and Systems*, 1, 014003, doi: [10.1117/1.JATIS.1.1.014003](https://doi.org/10.1117/1.JATIS.1.1.014003)

- Riello, M., De Angeli, F., Evans, D. W., et al. 2018, *A&A*, 616, A3, doi: [10.1051/0004-6361/201832712](https://doi.org/10.1051/0004-6361/201832712)
- Salz, M., Schneider, P. C., Czesla, S., & Schmitt, J. H. M. M. 2015, *A&A*, 576, A42, doi: [10.1051/0004-6361/201425243](https://doi.org/10.1051/0004-6361/201425243)
- Snedden, C. A. 1973, PhD thesis, THE UNIVERSITY OF TEXAS AT AUSTIN.
- Sousa, S. G., Adibekyan, V., Delgado-Mena, E., et al. 2021, *A&A*, 656, A53, doi: [10.1051/0004-6361/202141584](https://doi.org/10.1051/0004-6361/202141584)
- Southworth, J. 2012, *MNRAS*, 426, 1291, doi: [10.1111/j.1365-2966.2012.21756.x](https://doi.org/10.1111/j.1365-2966.2012.21756.x)
- Spina, L., Meléndez, J., Karakas, A. I., et al. 2018, *MNRAS*, 474, 2580, doi: [10.1093/mnras/stx2938](https://doi.org/10.1093/mnras/stx2938)
- Tejada Arevalo, R. A., Winn, J. N., & Anderson, K. R. 2021, *ApJ*, 919, 138, doi: [10.3847/1538-4357/ac1429](https://doi.org/10.3847/1538-4357/ac1429)
- Thiabaud, A., Marboeuf, U., Alibert, Y., Leya, I., & Mezger, K. 2015, *A&A*, 574, A138, doi: [10.1051/0004-6361/201424868](https://doi.org/10.1051/0004-6361/201424868)
- Tody, D. 1986, Society of Photo-Optical Instrumentation Engineers (SPIE) Conference Series, Vol. 627, The IRAF Data Reduction and Analysis System, ed. D. L. Crawford, 733, doi: [10.1117/12.968154](https://doi.org/10.1117/12.968154)
- . 1993, Astronomical Society of the Pacific Conference Series, Vol. 52, IRAF in the Nineties, ed. R. J. Hanisch, R. J. V. Brissenden, & J. Barnes, 173
- Torra, F., Castañeda, J., Fabricius, C., et al. 2021, *A&A*, 649, A10, doi: [10.1051/0004-6361/202039637](https://doi.org/10.1051/0004-6361/202039637)
- Trifonov, T., Tal-Or, L., Zechmeister, M., et al. 2020, *A&A*, 636, A74, doi: [10.1051/0004-6361/201936686](https://doi.org/10.1051/0004-6361/201936686)
- Turner, J. D., Pearson, K. A., Biddle, L. I., et al. 2016, *MNRAS*, 459, 789, doi: [10.1093/mnras/stw574](https://doi.org/10.1093/mnras/stw574)
- van Saders, J. L., Ceillier, T., Metcalfe, T. S., et al. 2016, *Nature*, 529, 181, doi: [10.1038/nature16168](https://doi.org/10.1038/nature16168)
- Virtanen, P., Gommers, R., Oliphant, T. E., et al. 2020, *Nature Methods*, 17, 261, doi: [10.1038/s41592-019-0686-2](https://doi.org/10.1038/s41592-019-0686-2)
- Wang, S.-i., Hildebrand, R. H., Hobbs, L. M., et al. 2003, in Society of Photo-Optical Instrumentation Engineers (SPIE) Conference Series, Vol. 4841, Instrument Design and Performance for Optical/Infrared Ground-based Telescopes, ed. M. Iye & A. F. M. Moorwood, 1145–1156, doi: [10.1117/12.461447](https://doi.org/10.1117/12.461447)
- Wenger, M., Ochsenbein, F., Egret, D., et al. 2000, *A&AS*, 143, 9, doi: [10.1051/aas:2000332](https://doi.org/10.1051/aas:2000332)
- Yana Galarza, J., Meléndez, J., Lorenzo-Oliveira, D., et al. 2019, *MNRAS*, 490, L86, doi: [10.1093/mnrasl/slz153](https://doi.org/10.1093/mnrasl/slz153)
- Yi, S., Demarque, P., Kim, Y.-C., et al. 2001, *ApJS*, 136, 417, doi: [10.1086/321795](https://doi.org/10.1086/321795)
- Yi, S. K., Kim, Y.-C., & Demarque, P. 2003, *ApJS*, 144, 259, doi: [10.1086/345101](https://doi.org/10.1086/345101)
- York, D. G., Adelman, J., Anderson, John E., J., et al. 2000, *AJ*, 120, 1579, doi: [10.1086/301513](https://doi.org/10.1086/301513)